



ELSEVIER



CrossMark

Available online at www.sciencedirect.com

ScienceDirect

Proceedings of the Combustion Institute 35 (2015) 1157–1166

**Proceedings
of the
Combustion
Institute**

www.elsevier.com/locate/proci

Numerical and experimental investigation of turbulent DME jet flames

Ankit Bhagatwala^{a,*}, Zhaoyu Luo^b, Han Shen^c, Jeffrey A. Sutton^c,
Tianfeng Lu^b, Jacqueline H. Chen^a

^a Combustion Research Facility, Sandia National Laboratories, Livermore, CA 94550, USA

^b Department of Mechanical Engineering, University of Connecticut, Storrs, CT 06269, USA

^c Department of Mechanical and Aerospace Engineering, The Ohio State University, Columbus, OH 43210, USA

Available online 26 June 2014

Abstract

Results are presented here from a three-dimensional direct numerical simulation of a temporally-evolving planar slot jet flame and experimental measurements within a spatially-evolving axisymmetric jet flame operating with DME (dimethyl ether, CH_3OCH_3) as the fuel. Both simulation and experiment are conducted at a Reynolds number of 13050. The Damköhler number, stoichiometric mixture fraction and fuel and oxidizer compositions also are matched between simulation and experiment. Simultaneous $\text{OH}/\text{CH}_2\text{O}$ PLIF imaging is performed experimentally to characterize the spatial structure of the turbulent DME flames. The simulation shows a fully burning flame initially, which undergoes partial extinction and subsequently, reignition. The scalar dissipation rate (χ) increases to a value much greater than that calculated from near-extinction strained laminar flames, leading to the observed local extinction. As the turbulence decays, the local values of χ decrease and the flame reignites. The reignition process appears to be strongly dependent on the local χ value, which is consistent with previous results for simpler fuels. Statistics of OH and CH_2O are compared between simulation and experiment and found to agree. The applicability of $\text{OH}/\text{CH}_2\text{O}$ (formaldehyde) product imaging as a surrogate for peak heat release rate is investigated. The concentration product is found to predict peak heat release rate extremely well in the simulation data. When this product imaging is applied to the experimental data, a similar extinction/reignition pattern also is observed in the experiments as a function of axial position. A new 30-species reduced chemical mechanism for DME was also developed as part of this work. Published by Elsevier Inc. on behalf of The Combustion Institute.

Keywords: DNS; Multi-scalar PLIF imaging; Non-premixed; DME; Extinction-reignition

1. Introduction

Non-premixed combustion is employed in diverse areas of application ranging from diesel

engines to gas turbines for power generation and aviation. One of the main challenges to using this mode of combustion for energy generation is flame stability. The high Reynolds numbers found in most industrial applications generate significant flame-turbulence interactions which may result in a partial or complete blow off, decreasing

* Corresponding author.

E-mail address: abhagat@sandia.gov (A. Bhagatwala).

efficiency and increasing unburned hydrocarbon emissions. It is therefore important to understand the details of this process. This requires a carefully designed simulation/experiment that involves partial flame extinction due to strong turbulence. With this objective, a 3-D Direct Numerical Simulation (DNS) and experiment of a turbulent DME jet flame undergoing extinction and reignition are performed. The DNS configuration is a three-dimensional, non-premixed, temporally-evolving slot jet flame, whereas, the experiment consists of a spatially-evolving, axisymmetric jet flame. Both DNS and experiment were performed at a jet Reynolds number of 13050 and Damköhler number of 0.08. The stoichiometric mixture fraction and composition of the fuel and oxidizer streams were also matched between DNS and experiment. The temporally-evolving configuration for the DNS was chosen over the spatially-evolving configuration because it allows the examination of processes such as local extinction that typically occur sufficiently downstream of the jet nozzle by invoking Taylor's hypothesis with much lower computational expense. Previous DNS studies using this configuration were focused on parametric variation in Reynolds number [1] and Damköhler number [2] and their effects on extinction and reignition. The focus of this study is a comparison of scalar statistics between simulation and experiment under similar conditions.

Given the differences in the geometry between the simulation and experiment, a direct one-to-one comparison between the DNS and experiments is not possible. However, both have been designed to lie in the same turbulence and thermochemical parameter space by matching the jet Reynolds number and global Damköhler number. Therefore, it is reasonable to expect that the statistics of thermochemical evolution for both flames should be comparable. The paper is organized as follows: Section 2 describes the simulation setup, numerical methods and problem parameters. Section 3 discusses the experimental setup and details of the imaging techniques. Section 4.1 describes results pertaining to flame evolution and its extinction and reignition from the DNS. Section 4.2 deals with the comparison between DNS and the experiment, in particular the joint statistics of OH and CH_2O and their utility in predicting peak heat release rate from experimental data. Section 5 draws conclusions from the study and directions for future work.

2. Numerical implementation

2.1. DNS code details

The DNS code used in this study is called S3D, a massively parallel compressible reacting flow solver developed at Sandia National Laboratories

[3]. S3D solves the fully compressible Navier–Stokes equations: total energy, species and continuity equations in conservative form with detailed chemistry. The spatial derivatives are computed on an equispaced, finite difference grid using eighth-order centered finite differences [4]. A tenth-order de-aliasing filter is applied every 10 time steps to remove high-wavenumber noise. The solution is integrated in time with a six-stage, fourth-order Runge–Kutta method [5]. A uniform grid is employed for this simulation with a grid spacing of 25 microns in all directions to adequately resolve all radical layers as well as the mean Kolmogorov scale.

2.2. Initial and boundary conditions

The jet is initialized as two shear layers with a streamwise velocity $\Delta U/2$ in the center of the jet (fuel stream) and $-\Delta U/2$ outside it (oxidizer coflow), as shown in Fig. 1 (top plot). Turbulent fluctuations are initialized as a field of isotropic turbulence superimposed on top of the mean velocity in the jet region and filtered outside of it. The fuel core width H_z is initialized to have a greater width than the jet. This is to allow the artificial turbulence to trip the Kelvin–Helmholtz instability in the shear layer and evolve into fully developed sheared turbulence before it interacts with the mixing layer. Jet parameters for this problem are given in Table 1. The fuel jet is comprised of 12% DME, 18% H_2 and 70% N_2 by volume while the oxygen enriched oxidizer stream is comprised of 31% O_2 and 69% N_2 . These compositions were chosen to achieve a sufficient extinction dissipation rate (χ_q) so as to achieve a larger Damköhler number, given by $Da = \chi_q t_j$, where $t_j = D/\Delta U$, so that the flame is able to sustain a burning state at the simulated Reynolds number. The stoichiometric mixture fraction for this composition profile, $Z_{st} = 0.375$, is such that the stoichiometric surface is located in a region of high turbulent shear. The initial profile is chosen from a near-extinction laminar strained flame solution from OPPDIF [6], where the peak scalar dissipation rate is approximately 75% of the laminar extinction value of $1950 s^{-1}$. The boundary conditions are periodic in the streamwise and spanwise directions, and non-reflecting outflow in the transverse direction. The outflow boundary condition was implemented with the NSCBC method [7].

2.3. Reduced chemical mechanism for DME

The present reduced mechanisms for DME oxidation were developed from the detailed mechanism by Zhao et al. [8], which consists of 55 species and 290 elementary reactions. A brief synopsis of the mechanism reduction is described here. A detailed validation for reduction is

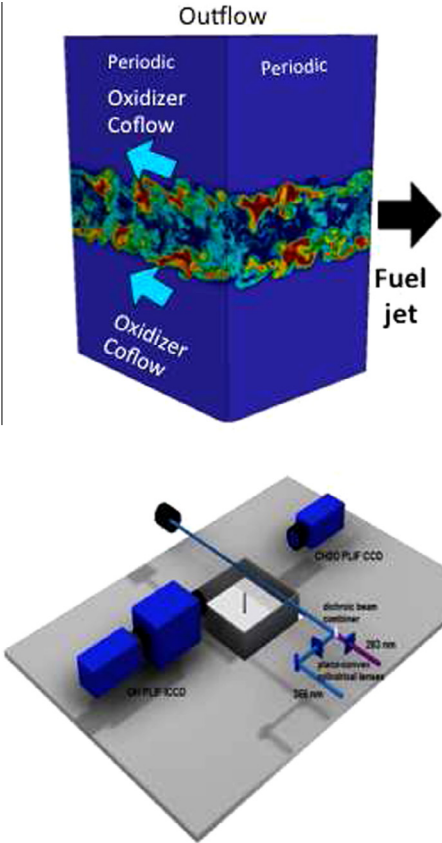


Fig. 1. Schematic of the DNS domain (top); and the experimental setup (bottom).

Table 1
Simulation and experimental parameters. Da is defined as $\chi_q t_f$ where $t_f = D/\Delta U$ is the jet time scale and χ_q is the extinction dissipation rate for a 1D strained laminar flame at the same composition. Jet Reynolds number for DNS is defined based on the hydraulic diameter defined as $D = 2L_z H / (L_z + H)$ where H is the jet width and L_z is the spanwise extent of the domain. Simulation domain extents are $(L_x, L_y, L_z) = (10H, 16H, 8H)$.

Parameter	DNS	Expt.
Jet Reynolds number, Re_{jet}	13050	13050
Jet width, H (mm)	2.3	N/A
Hydraulic diameter, D (mm)	4.1	3.43
Jet velocity, ΔU (m/s)	98	57
Fuel core width, HZ (mm)	3.6	N/A
Pressure, P (atm)	1.0	1.0
Damkohler number, Da	0.08	0.074
Stoichiometric mixture fraction, Z_{st}	0.375	0.375
Unburnt temperature, T_u (K)	450	298
Burnt temperature, T_b (K)	2380	2299
Extinction dissipation rate, χ_q (s^{-1})	1950	1210

provided as supplementary material. The chemical stiffness associated with the short timescales of the highly reactive radicals in the detailed mechanisms renders it infeasible to apply the detailed

mechanisms in S3D when the efficient explicit integration solvers are used [9,10]. Therefore, a non-stiff reduced mechanism with 30 species and 175 reactions was developed for efficient explicit time integration in the DNS. The reduction was based on reaction states sampled in a wide range of pressures, temperatures and equivalence ratios. First, the method of directed relation graph (DRG) [11] and DRG-aided sensitivity analysis (DRGASA) [12,13] were applied to eliminate unimportant species and reactions from the detailed mechanism, and a 39 species skeletal mechanism was obtained. Second, linearized quasi-steady state approximations (LQSSA) [14] were applied to the 39 species skeletal mechanism to further reduce the number of transported species. Using a criterion based on computational singular perturbation (CSP) [15], 9 species, namely CH_2 , CH_2^* , C_2H_3 , HCO , CH_2OH , CH_3OCH_2 , $HOCH_2O$, CH_3OCH_2O , and $CH_2OCH_2O_2H$, were identified as global QSS species. The algebraic equations associated with the QSS species were analytically solved for high numerical efficiency and robustness. Third, the method of diffusive species bundling [16] was utilized to group the species into 14 diffusive groups to facilitate the evaluation of the mixture-averaged species diffusion. Finally, the method of dynamic stiffness removal [9] was employed to eliminate the chemical timescales shorter than 10 ns, resulting in a 30-species non-stiff reduced mechanism.

3. Experimental methods

3.1. Flame conditions

The jet flames considered experimentally are axisymmetric, which flow from a 3.43-mm-diameter nozzle into a 30 cm \times 30 cm low-speed (0.3 m/s) co-flowing oxidizer stream. The fuel (12% DME, 18% H_2 and 70% N_2) and oxidizer streams (31% O_2 and 69% N_2) match the DNS compositions. Both the fuel and the oxidizer streams are initially at 298 K in the experiment as compared to 450 K in the simulation. All fuel constituents issue from compressed gas cylinders, which are metered with digital mass flow controllers with an accuracy of $\pm 0.8\%$ after in-house calibration with a laminar flow element (Meriam Process Technologies).

While the specific DNS and experimental configurations are different (temporally-evolving planar jet vs. spatially-evolving axisymmetric jet), the jet Reynolds and Damköhler (Da) numbers of the experiment were designed to match the DNS as shown in Table 1, thus facilitating statistical comparisons and general conclusions concerning turbulence-chemistry interaction characteristic of DME flames. Matching Da and Re_{jet} across experiment and DNS is critical and was achieved

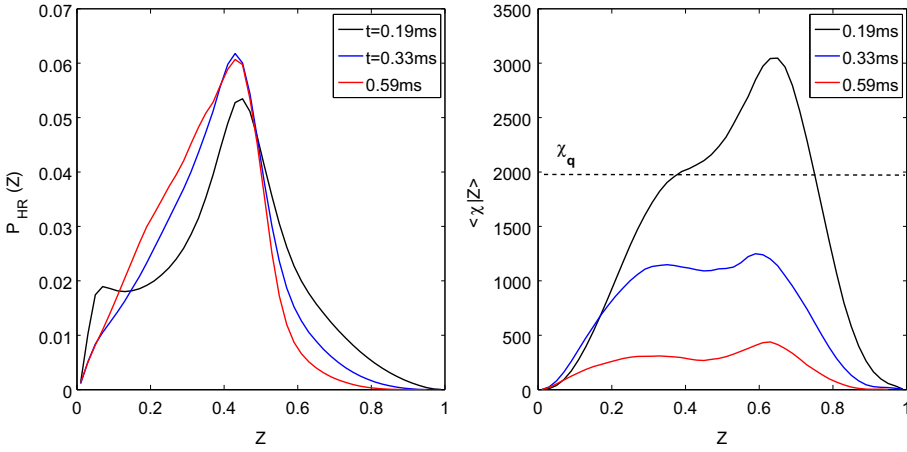


Fig. 2. PDF of mixture fraction weighted by heat release rate (left), conditionally averaged scalar dissipation rate (right).

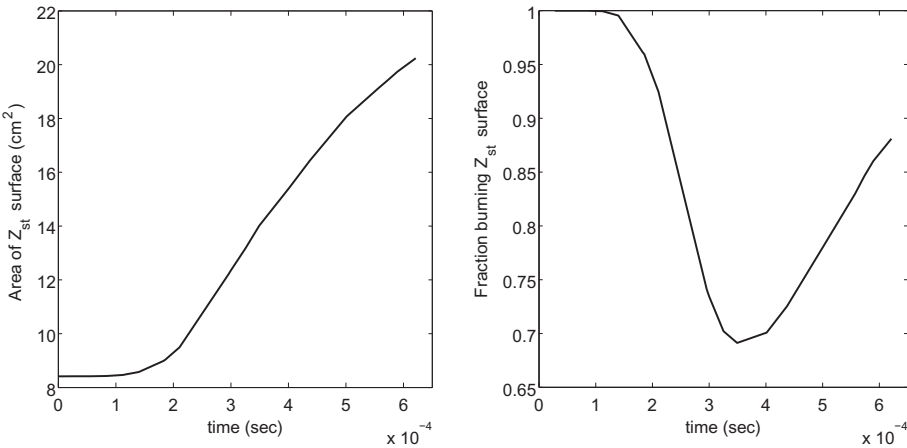


Fig. 3. Area of stoichiometric surface (left), fraction of stoichiometric surface burning (right).

by selecting a nozzle diameter (D) such that these criteria were satisfied. Similar to the DNS, the experimental Da is defined as $DU^{-1}\chi_q$, where U is the jet exit velocity and χ_q is the extinction scalar dissipation rate for a one-dimensional strained laminar flame at the same composition as the experiment. The Da also can be written in terms of the jet Reynolds number as $D^2(Re_{jet}v)^{-1}\chi_q$. By enforcing $Da_{exp} = Da_{DNS}$ and $Re_{jet,exp} = Re_{jet,DNS}$, the required D is calculated as

$$D = D_{DNS} \left(\frac{\chi_{q,DNS}}{\chi_{q,exp}} \right)^{1/2} \left(\frac{v(T)_{exp}}{v(T)_{DNS}} \right)^{1/2} \quad (1)$$

3.2. Laser diagnostic techniques

Simultaneous OH and CH_2O planar laser-induced fluorescence (PLIF) measurements were

performed within the turbulent jet flames using two temporally-synched laser and camera systems as shown in Fig. 1 (bottom plot). The first laser system consisted of an Nd:YAG-pumped dye laser which was frequency-doubled via a type-I BBO crystal to 283.636 nm (vacuum) for the OH PLIF measurements. The measured spectral line-width was 0.12 cm^{-1} . The 283.636 nm wavelength corresponds to excitation of the $Q1(8)$ rotational line of the $A^{2\Sigma^+} \leftarrow X^2\Pi(1,0)$ band of OH . This rotational line was selected for its minimal temperature sensitivity, which leads to relative PLIF signals that are closely proportional to relative OH concentrations or mole fractions. For example, based on 1D counterflow flame calculations, the selection of the $Q1(8)$ rotational line leads to relative OH PLIF signals that are on average within 10% and 6% of the relative OH molar concentration and OH mole fraction profiles, respectively.

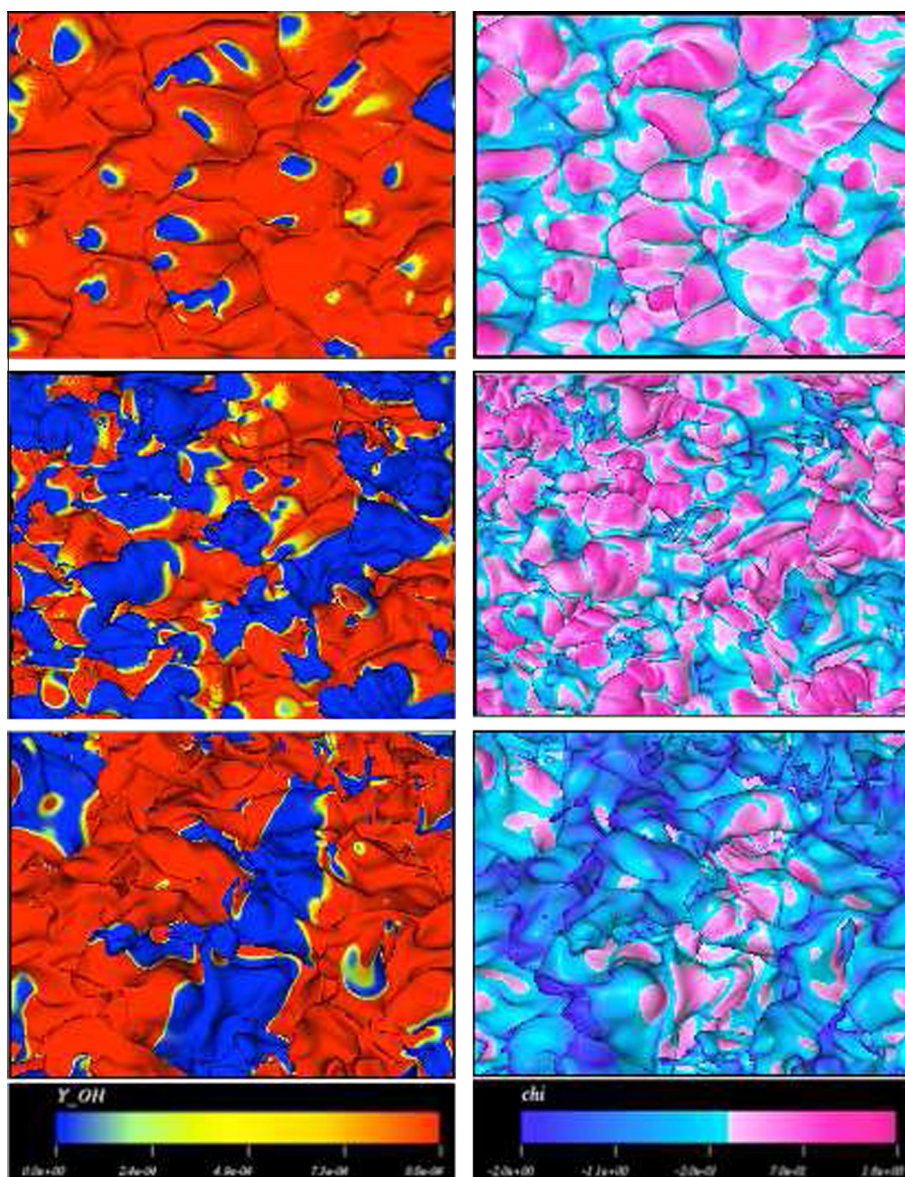


Fig. 4. Stoichiometric mixture fraction isosurfaces at $t = 0.18$ ms (top); $t = 0.32$ ms (middle); $t = 0.6$ ms (bottom). Colored by OH mass fraction (left) and $\log(\chi/\chi_q)$ (right). For the OH plot, red represents burning regions and blue represents extinguished regions. For the χ plot, pink represents regions of high χ and blue represents regions of low χ . $\log(\chi/\chi_q)$ ranges from -2 to 1.6 in the plot. (For interpretation of the references to colour in this figure legend, the reader is referred to the web version of this article.)

The second laser system consisted of a frequency-tripled, injection-seeded, Nd:YAG laser (Spectra Physics Pro 290) outputting > 500 mJ/pulse at 355 nm for the excitation of transition of CH_2O . The narrow spectral linewidth (~ 100 MHz) of the injection-seeded laser is advantageous as it has been shown in our laboratory that increased CH_2O fluorescence levels (up to $2\times$) are achieved with narrowband excitation. The 355-nm output is

horizontally-polarized to negate Rayleigh and Raman scattering contributions. Both the 283-nm and 355-nm laser beams are formed into 2D laser sheets with separate combinations of plano-concave cylindrical and plano-convex spherical lenses. The 283-nm output is formed into a $50\text{ mm} \times 0.32\text{ mm}$ laser sheet, while the 355-nm output is formed into a $40\text{ mm} \times 0.2\text{ mm}$ laser sheet. The two laser sheets are combined via a

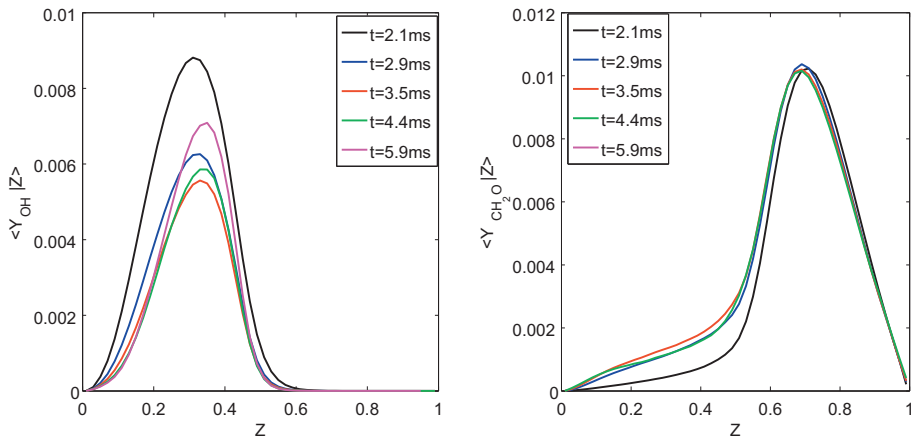


Fig. 5. Conditionally averaged mass fractions of OH (left), CH_2O (right) conditioned on mixture fraction.

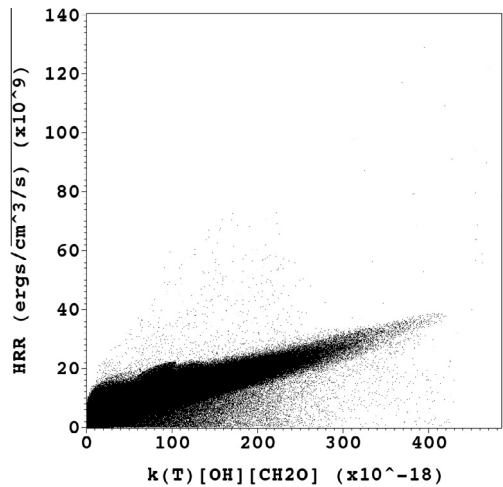


Fig. 6. Scatter plot for heat release rate (HRR) versus R_{OH} from the DNS data.

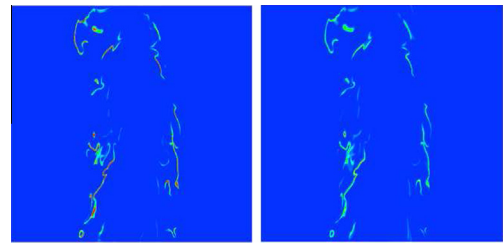


Fig. 7. Slices at spanwise midplane for R_{OH} (left) and heat release rate (right) at $t = 0.6$ ms from DNS.

dichroic beam splitter and overlapped within the test section to $\pm 50\text{ }\mu\text{m}$.

The OH emission from the $A-X(1,1), (0,0)$ and $B-X(0,1)$ bands between 306 nm and

320 nm was detected by a lens-coupled ICCD camera system (PCO Sensicam CCD + LaVision IRO) outfitted with an $f/1.8$, 100-mm focal length UV camera lens (Cercio) and the combination of a WG305 longpass filter and UG 11 bandpass filter to eliminate 283 nm Rayleigh scattering, flame luminosity, and CH_2O fluorescence crosstalk. The CH_2O emission from electronic transition between 380 nm and 500 nm was collected by an un-intensified scientific-grade CCD camera (PCO Sensicam) outfitted with an $85\text{-mm } f/1.4$ Nikon camera lens and Schott GG380 longpass filter. Rayleigh and Raman scattering interferences are negligible due to the combination of horizontal polarization and the GG380 longpass filter. The optical magnification of the OH PLIF camera is 0.22 , corresponding to an imaged pixel size of $61\text{ }\mu\text{m}$ (after 2×2 pixel binning). The optical magnification of the CH_2O PLIF camera is 0.25 , corresponding to an imaged pixel size of $52\text{ }\mu\text{m}$ (after 2×2 pixel binning). The two different camera systems were subsequently mapped onto a common field-of-view and magnification via the DaVis software. The master clock of the system was the free-running OH PLIF laser, which triggered a digital delay generator (Stanford Systems DG645), which then triggered the CH_2O laser and the two camera systems. Due to jitter in the OH PLIF laser, the two cameras are slightly asynchronous, with temporal overlaps of $\pm 600\text{ ns}$. However, this temporal uncertainty only corresponds to relative image mismatch or blur of 0.5 pixels for the highest velocities considered. Eight hundred OH/CH_2O image pairs are collected at seven axial locations corresponding to axial positions of $8 < x/D < 35$. Finally it is noted that the simultaneous OH/CH_2O images can be used to infer the locations of the peak heat release rate through the $OH \times CH_2O$ PLIF technique as described in [17,18].

4. Results

4.1. DNS flame evolution

The simulation was run for 0.6 milliseconds or $15t_f$. The imposed initial condition results in a contiguous reaction sheet with peak heat release rate occurring at a mixture fraction that is slightly rich of stoichiometric as seen in Fig. 2 which shows the heat release weighted PDF of mixture fraction defined as $P_{HR}(Z) = \langle HRR | Z \rangle P(Z) / \langle HRR \rangle$. This quantity also can be interpreted as a normalized aggregate heat release rate conditioned on the mixture fraction. As the jet develops, the fully burning flame is enveloped in a region of high strain rate and scalar dissipation rate, which partially extinguishes it. As the turbulent fluctuations decay, the strain rate (not shown) and hence the scalar dissipation rate decrease monotonically at all mixture fraction levels as seen in Fig. 2, and subsequently the extinguished regions of the flame reignite.

Figure 3 shows the area of the stoichiometric mixture fraction surface and the fraction of the burning stoichiometric surface area in the domain. The fraction was computed based on a OH mass fraction threshold chosen to be 75% of its laminar value near extinction. As the strong turbulent mixing wrinkles and distorts the mixture fraction contours, the area of the stoichiometric isosurface is seen to continuously increase with time. The burning fraction reaches a minimum of around 70% due to local extinction, and subsequently increases as the flame re-ignites.

Figure 4 shows a plan view of the stoichiometric mixture fraction isosurface colored by the OH mass fraction threshold (75% of laminar extinction value) at three representative time instances. Red represents burning regions while blue repre-

sents extinguished regions. The three phases noted above are evident from the plots. At $t = 0.18$ ms local extinction is starting to occur, and the OH plot shows a partially broken reaction sheet. Small holes begin to form on the flame surface, with curvature convex towards the oxidizer stream, and propagate outwards. By $t = 0.32$ ms near the peak level of extinction, the thresholded OH field shows a highly fragmented flame, corresponding to the time of maximum extinction shown in Fig. 3. By $t = 0.6$ ms, a strongly reigniting flame has been established. The scalar dissipation rate conditioned on the stoichiometric surface is also shown in Fig. 4. The large values of χ observed early in the development leads to the considerable extinction observed at $t = 0.32$ ms. Peak values of χ are about a factor of 100 in excess of the laminar extinction value. During the reignition phase (bottom plot), it is seen that regions with higher values of χ correspond to extinction holes and those with lower χ values correspond to burning regions. As the scalar dissipation rate decreases, the flame is observed to reignite (bottom plot), although local pockets of high χ persist, preventing the flame from re-igniting fully by this time. These results are consistent with previous experimental and numerical work that have shown the importance of the scalar dissipation rate at the stoichiometric surface on local flame extinction [19,1,2].

Two species that play a key role in the extinction and reignition process are OH and CH_2O . Figure 5 plots conditionally averaged OH and CH_2O mass fractions at different time instances before extinction, during extinction and during reignition. It can be seen that OH peaks slightly on the lean side and decreases during extinction, then increases during reignition. CH_2O peaks on

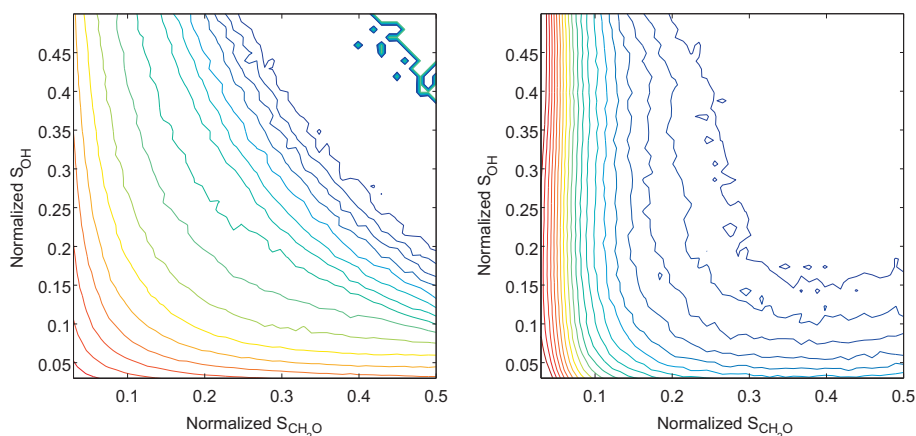


Fig. 8. Overlap conditioned joint PDFs of OH and CH_2O signal intensities derived from their respective mole fractions for DNS (left) and their signal intensities from experiment (right). Same contour levels were used for both plots. Overlap was taken to correspond with values between 1% and 50% of the maximum respective signal intensity for both DNS and experiment.

the rich side and has a behavior opposite to OH near the peak heat release point at the stoichiometric mixture fraction. It increases during extinction and decreases during reignition through consumption reactions.

4.2. OH/CH_2O product imaging

Paul and Najm [17] first showed that the product of concentrations of OH and CH_2O show excellent spatio-temporal correlation with peak heat release rate in a laminar methane-air flame. This product is directly related to the forward reaction rate of the reaction $CH_2O + OH \rightarrow H_2O + HCO$, given by $R_{OH} = k_f(T)[OH][CH_2O]$ where the

forward rate constant is taken to be $k_f(T) = 5.7 \times 10^{-17} T^{1.18} \exp(225/T)$ [17]. Figure 6 shows the correlation between the computed total heat release rate and the reaction rate from the DME DNS data at $t = 0.19$ ms. The correlation coefficient was found to be 0.9 and the maximum conditional variance was found to be 5%. Although not shown here, this level of correlation was seen at later times as well. The good correlation between this product and heat release rate was also noted in [20].

This product is compared with an instantaneous realization of heat release rate at one time instant during the reignition phase in the simulation. Figure 7 shows slices of R_{OH} and heat release

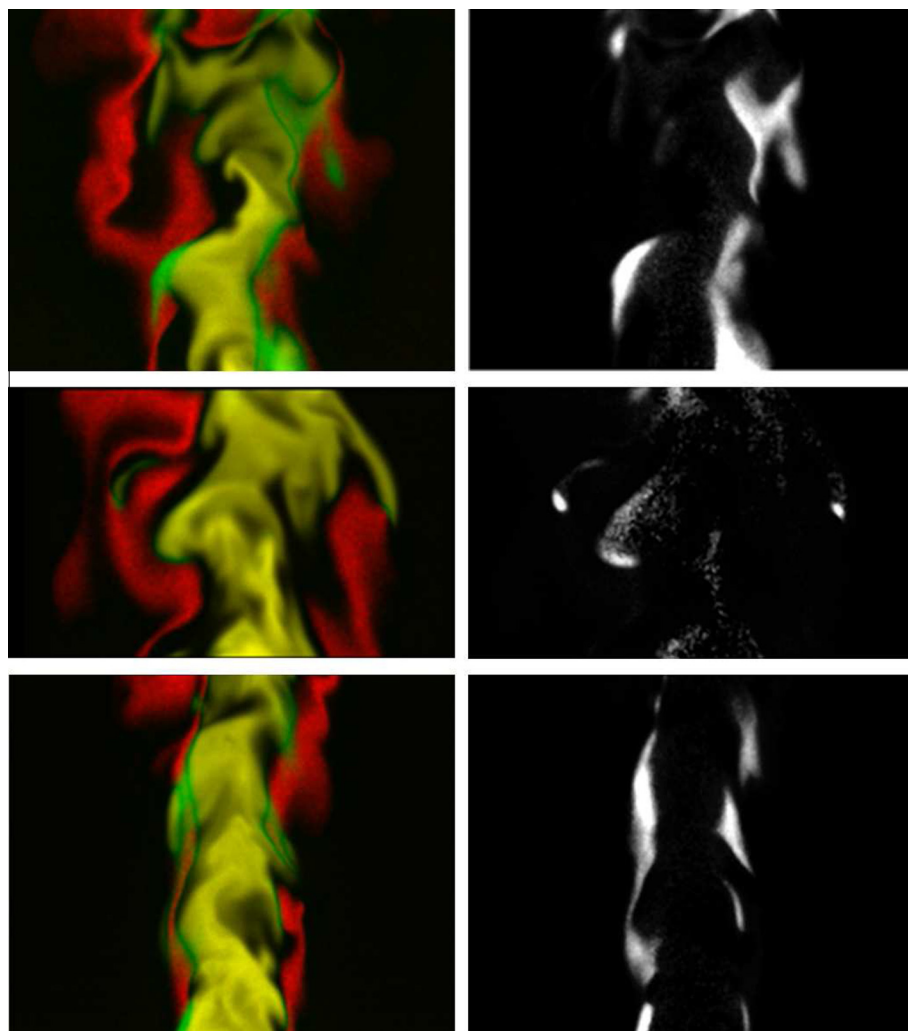


Fig. 9. Simultaneous rendering of OH/CH_2O PLIF (left) and R_{OH} product imaging (right). Quantity plotted in the right column is R_{OH} , which is proportional to $k_f [CH_2O][OH]$. $x/d = 20$ (bottom), $x/d = 25$ (middle), and $x/d = 30$ (top). The Black \rightarrow Yellow color scheme is CH_2O and the Black \rightarrow Red color scheme is OH . The green rendering indicates regions of strong overlap. (For interpretation of the references to colour in this figure legend, the reader is referred to the web version of this article.)

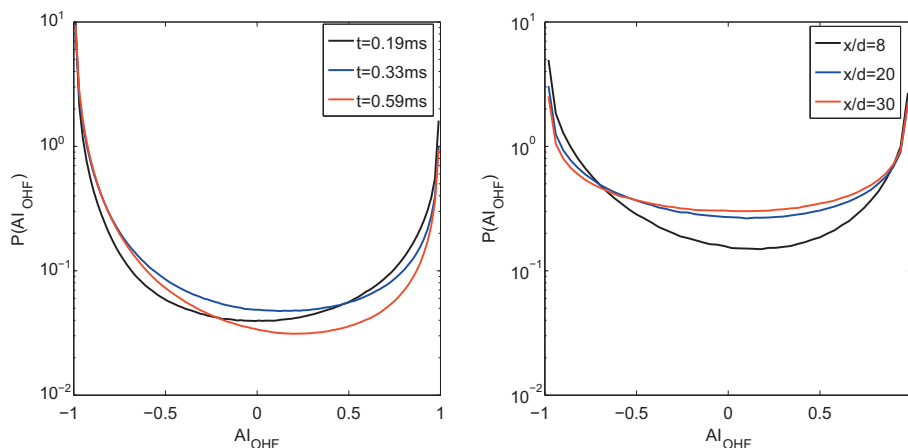


Fig. 10. PDF of the alignment index between OH and CH_2O for the DNS (left) and experiment (right).

rate taken at the midplane in the spanwise direction. The product correlates extremely well with peak heat release rate corresponding to near stoichiometric conditions. This correlation is observed during the extinction phase as well (not shown). It is not able to capture the lower intensity heat release on the lean and rich sides. This was examined through a reaction flux analysis which showed that exothermic reactions involving OH and CH_2O occur predominantly on the lean and rich sides respectively. This results in low concentrations of OH on the rich side and CH_2O on the lean side, making R_{OH} a poor indicator of heat release away from the stoichiometric surface. Najm et al. [20] noted that the product of H and CH_2O may be a better candidate for a heat release surrogate; however, it suffers from the drawback that H is not easily observable in experiments. Nevertheless, since both OH and CH_2O are simultaneously measured in the current experiment, their product is a useful measure of peak heat release rate.

Figure 8 plots the log of the joint PDF of OH and CH_2O signal intensities derived from their respective mole fractions in the simulation and the signal intensities observed in the experiment. The PDF is conditioned such that only points in the overlap region are considered, since this is the region of interest from the point of view of predicting heat release. This was taken to correspond to values between 1% and 50% of the maximum respective signal intensity for the experiment and for the DNS. It should be noted that the joint PDFs should not be expected to be identical due to the different geometries of the DNS and experiment. Furthermore, in the experiment overlap occurs at very low values, near the experimental measurement threshold. Nevertheless, it is seen that both joint PDFs exhibit the same functional form, i.e. there exists a strong anti-correlation between OH and CH_2O . Whereas OH is located pri-

marily in burning regions, CH_2O is found primarily in non-burning regions.

Figure 9 shows instantaneous realizations of simultaneous OH/CH_2O and R_{OH} measurements at different downstream locations. Even though direct comparison with the simulation results is not possible, these locations were chosen to correspond to the three phases identified in the DNS, i.e. burning, partially-extinguished and reigniting. These stages compare well with the snapshots from the simulation in a qualitative sense.

To further quantify the degree of anti-correlation between OH and CH_2O , an alignment index is defined between gradients of OH and CH_2O as

$$AI_{OHF} = \frac{\nabla Y_{OH} \cdot \nabla Y_{CH_2O}}{|\nabla Y_{OH}| |\nabla Y_{CH_2O}|} \quad (2)$$

A comparison of the PDF of this dot product for both experiment and DNS conditioned on the product $Y_{OH} \times Y_{CH_2O}$ being non-zero is shown in Fig. 10. In both cases, the PDF peaks at -1 at all time instances in the DNS and spatial locations in the experiment, indicating that the gradients of OH and CH_2O are opposed and that the trends from the DNS and the experiment agree.

5. Conclusions

DNS of a temporally-evolving planar slot jet flame with DME has been conducted and compared with an experimental spatially-evolving axisymmetric DME jet flame. While the specific geometries of the DNS and the experiment are different, the jet Reynolds and Damköhler (Da) numbers of the experiment were designed to match the DNS, thus facilitating statistical comparisons. A new 30 species reduced chemical mechanism has been developed for DME. The

simulation shows a fully burning flame which partially extinguishes and eventually reignites. The sheared turbulence eventually decays, leading to a decrease in the local scalar dissipation rate, which aids in flame reignition. Joint statistics of OH and CH_2O are compared between simulation and experiment and found to be in good agreement. ROH product imaging is evaluated as a surrogate for peak heat release rate and is found to be an excellent surrogate of the peak heat release rate in the simulation data. When applied to the experimental data, similar extinction and reignition phenomena are also observed in the experiment. Future work will focus on detailed comparisons of extinction hole size distributions and on quantifying the mechanism for reignition in DME jet flames.

Acknowledgements

The research at Sandia and Ohio State is supported by the Combustion Energy Frontier Research Center (CEFRC), an Energy Frontier Research Center funded by the U.S. Department of Energy (DOE), Office of Science, Office of Basic Energy Sciences (BES) under Award No. DE-SC0001198. Sandia is a multiprogram laboratory operated by Sandia Corporation, a Lockheed Martin Company, for the United States Department of Energy under Contract DE-AC04-94AL85000. The work at University of Connecticut was supported by the Office of Basic Energy Sciences, Office of Science, U.S. Department of Energy under Grant DE-SC0008622. Computer allocations were awarded by the Department of Energy's INCITE award at the Oak Ridge Leadership Computing Facility (OLCF) at the Oak Ridge National Laboratories (ORNL).

Appendix A. Supplementary material

Supplementary data associated with this article can be found, in the online version, at <http://dx.doi.org/10.1016/j.proci.2014.05.147>.

References

- [1] E.R. Hawkes, R. Sankaran, J.C. Sutherland, J.H. Chen, *Proc. Comb. Inst.* (31) (2007) 1633–1640.
- [2] D.O. Lignell, J.H. Chen, H.A. Schmutz, *Comb. Flame* (158) (2011) 949–963.
- [3] J.H. Chen, A. Choudhary, B. de Supinsky, M. DeVries, E.R. Hawkes, S. Klasky, W.K. Liao, K.L. Ma, J. Mellor-Crummey, N. Podhorski, R. Sankaran, S. Shende, C.S. Yoo, *Comp. Sci. Disc.* (2) (2009) 015001.
- [4] C.A. Kennedy, M.H. Carpenter, *Appl. Numer. Math.* (14) (1994) 397–433.
- [5] C.A. Kennedy, M.H. Carpenter, R.M. Lewis, *Appl. Numer. Math.* (35) (2000) 177–219.
- [6] R.J. Kee, F.M. Rupley, J.A. Miller, M.E. Coltrin, J.F. Grear, E. Meeks, H.K. Moffat, A.E. Lutz, G. Dixon-Lewis, M.D. Smooke, J. Warnatz, G.H. Evans, R.S. Larson, R.E. Mitchell, L.R. Petzold, W.C. Reynolds, M. Caracotsios, W.E. Stewart, P. Glarborg, C. Wang, O. Adigun, CHEMKIN Collection, Release 3.6, Reaction Design, Inc., San Diego, CA, 2000.
- [7] J.C. Sutherland, C.A.J. Kennedy, *Comput. Phys.* (191) (2003) 502–524.
- [8] Z. Zhao, M. Chaos, A. Kazakov, F. Dryer, *Int. J. Chem. Kinet.* (40) (2008) 1–18.
- [9] T.F. Lu, C.K. Law, C.S. Yoo, J.H. Chen, *Comb. Flame* (156) (2009) 1542–1551.
- [10] T.F. Lu, C.K. Law, *Prog. Energy Comb. Sci.* (35) (2009) 192–215.
- [11] T.F. Lu, C.K. Law, *Proc. Comb. Inst.* (30) (2005) 1333–1341.
- [12] X.L. Zheng, T.F. Lu, C.K. Law, *Proc. Comb. Inst.* (31) (2007) 367–375.
- [13] R. Sankaran, E.R. Hawkes, J.H. Chen, T. Lu, C.K. Law, *Proc. Comb. Inst.* (31) (2007) 1291–1298.
- [14] T.F. Lu, C.K. Law, *J. Phys. Chem. A* (110) (2006) 13202–13208.
- [15] T.F. Lu, C.K. Law, *Comb. Flame* (154) (2008) 761–774.
- [16] T.F. Lu, C.K. Law, *Comb. Flame* (148) (2007) 117–126.
- [17] P.H. Paul, H.N. Najm, *Proc. Comb. Inst.* (27) (1998) 43–50.
- [18] B. Ayyoola, R. Balachandran, J. Frank, E. Mastorakos, C. Kaminski, *Comb. Flame* (144) (2006) 1–16.
- [19] J.A. Sutton, J.F. Driscoll, *Proc. Comb. Inst.* (31) (2007) 1487–1495.
- [20] H.N. Najm, O.M. Knio, P.H. Paul, *Comb. Sci. Tech.* (140) (1998) 369–403.